LETTER

https://doi.org/10.1038/s41586-019-1428-4

Global entangling gates on arbitrary ion qubits

Yao Lu[1,3]*, Shuaining Zhang[1,3], Kuan Zhang[1,2,3], Wentao Chen[1], Yangchao Shen[1], Jialiang Zhang[1], Jing-Ning Zhang[1] & Kihwan Kim[1]*

Quantum computers can efficiently solve classically intractable problems, such as the factorization of a large number[1] and the simulation of quantum many-body systems[2,3]. Universal quantum computation can be simplified by decomposing circuits into single- and two-qubit entangling gates[4], but such decomposition is not necessarily efficient. It has been suggested that polynomial or exponential speedups can be obtained with global *N*-qubit (*N* greater than two) entangling gates[5–9]. Such global gates involve all-to-all connectivity, which emerges among trapped-ion qubits when using laser-driven collective motional modes[10–14], and have been implemented for a single motional mode[15,16]. However, the single-mode approach is difficult to scale up because isolating single modes becomes challenging as the number of ions increases in a single crystal, and multi-mode schemes are scalable[17,18] but limited to pairwise gates[19–23]. Here we propose and implement a scalable scheme for realizing global entangling gates on multiple $^{171}Yb^{+}$ ion qubits by coupling to multiple motional modes through modulated laser fields. Because such global gates require decoupling multiple modes and balancing all pairwise coupling strengths during the gate, we develop a system with fully independent control capability on each ion[14]. To demonstrate the usefulness and flexibility of these global gates, we generate a Greenberger–Horne–Zeilinger state with up to four qubits using a single global operation. Our approach realizes global entangling gates as scalable building blocks for universal quantum computation, motivating future research in scalable global methods for quantum information processing.

A representative entangling gate with more than two qubits is the global entangling gate, which can generate entanglement among all involved qubits in a symmetric way. A global entangling gate acting on N qubits is defined as

$$\mathrm{GE}_N(\Theta) = \exp\left(-i\Theta\sum_{j<j'}^{N}\sigma_x^j\sigma_x^{j'}\right) \quad (1)$$

where all of the two-body couplings are driven simultaneously with strength Θ, and σ_x^j is the Pauli operator on the jth qubit. A global entangling gate applied to N qubits is equivalent to $N(N-1)/2$ pairwise entangling gates[9], which provides the possibility of simplifying quantum circuits. For example, the N–1 pairwise entangling operations involved in the preparation of the N-qubit Greenberger–Horne–Zeilinger (GHZ) state[20,24] can be replaced by a single global entangling gate $\mathrm{GE}_N(\pi/4)$, as shown in Fig. 1a. In fact, several theoretical works have already indicated that numerous quantum algorithms and universal quantum simulations of various many-body systems would benefit from global entangling gates for the efficient construction of quantum circuits. In particular, a set of $O(N)$ controlled NOT gates in the quantum phase estimation algorithm[9]—as well as each $O(N)$–body interaction term that emerges in the simulation of fermionic systems owing to the Jordan–Wigner transformation[5,6], which requires $O(N)$ pairwise gates—can be efficiently implemented by $O(1)$ global gates. Moreover, because the global gate contains all of the pairwise couplings, we can flexibly apply it on any subset of the qubits involved by simply removing the couplings between certain qubits.

The global entangling gates demand fully connected couplings among all of the involved qubits, which naturally emerge in trapped-ion systems. Ion qubits in a linear chain are entangled by coupling to the collective motional modes, typically through Raman laser beams, as shown in Fig. 1b. Raman beams with beat-note frequencies $\omega_0 \pm \mu$ lead to a qubit-state-dependent force on each qubit site[25]. Here, μ, which has a value around the frequencies of the motional modes, is the detuning from the energy splitting of the qubit, ω_0, as shown in Fig. 1c. The time evolution of the system at time τ can be written as[18]

$$U(\tau) = \exp\left[\sum_{j,m}\beta_{j,m}(\tau)\sigma_x^j - i\sum_{j<j'}\theta_{j,j'}\sigma_x^j\sigma_x^{j'}\right] \quad (2)$$

with $\beta_{j,m}(\tau) = \alpha_{j,m}(\tau)\alpha_m^{\dagger} - \alpha_{j,m}^{*}(\tau)\alpha_m$, where a_m ($\alpha_m^{\dagger}$) is the annihilation (creation) operator of the mth mode, $\alpha_{j,m}$ represents the displacement of the mth motional mode of the jth ion (see Supplementary Information) and $\theta_{j,j'}(\tau)$ is the coupling strength between the jth and jth qubits and has the form

$$\theta_{j,j'}(\tau) = -\sum_m\int_0^{\tau}\mathrm{d}t_2\int_0^{t_2}\mathrm{d}t_1\frac{\eta_{j,m}\eta_{j',m}\Omega_j(t_2)\Omega_{j'}(t_1)}{2}\sin\{(\nu_m-\mu)(t_2-t_1) - [\phi_j(t_2)-\phi_{j'}(t_1)]\} \quad (3)$$

where $\eta_{j,m}$ is the scaled Lamb–Dicke parameter, ν_m is the frequency of the mth motional mode, and $\Omega_j(t)$ and $\phi_j(t)$ are the amplitude and the phase of the carrier Rabi frequency on the jth ion, respectively.

The implementation of global entangling gates would be straightforward if we could only drive the centre-of-mass (COM) mode either in the axial or in the radial direction[10,15,16]. The homogeneous ion–motion couplings of the COM modes, $\eta_{j,1} = \eta_{\mathrm{COM}}$, make all of the coupling strengths uniform as

$$\theta_{j,j'}(\tau) = -\frac{\eta_{\mathrm{COM}}^2\Omega^2\tau}{2(\nu_1-\mu)} \quad (4)$$

by ensuring that $\alpha_{j,1}(\tau) = 0$ at time τ with the conditions $\Omega_j(t) = \Omega$ and $\phi_j(t) = 0$ for all of the ions. However, owing to the bunching of an increasing number of motional modes and their crosstalk when the number of ions increases, we have to dramatically slow down the gate speed to isolate the COM mode[20]. Otherwise, inevitably the rest of the modes are also driven. Either of these effects would decrease the gate fidelity, owing to the limited coherence time or undesired inhomogeneous couplings (see details in Methods), as shown in Fig. 1d. Moreover, the COM modes suffer from more severe electrical noise compared with other modes, and the heating rates increase with the number of ions[26], which would further degrade the gate fidelity.

Owing to the lack of scalability of the single-mode approach, we explore the possibility of finding multi-mode schemes for a scalable global N-qubit entangling gate. To apply the global gate $\mathrm{GE}_N(\Theta)$ in

[1]Center for Quantum Information, Institute for Interdisciplinary Information Sciences, Tsinghua University, Beijing, China. [2]MOE Key Laboratory of Fundamental Physical Quantities Measurement & Hubei Key Laboratory of Gravitation and Quantum Physics, PGMF and School of Physics, Huazhong University of Science and Technology, Wuhan, China. [3]These authors contributed equally: Yao Lu, Shuaining Zhang, Kuan Zhang. *e-mail: yao-lu14@mails.tsinghua.edu.cn; kimkihwan@mail.tsinghua.edu.cn

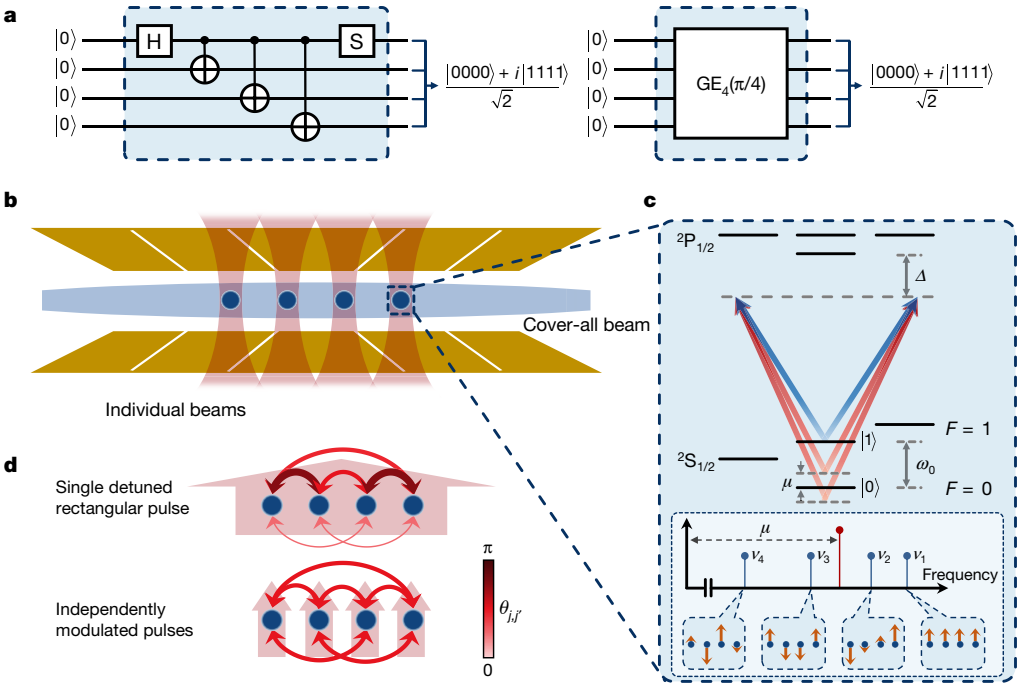

Fig. 1 | Global entangling gate and its experimental implementation. **a**, Efficient construction of a quantum circuit using a global gate. For the generation of the four-qubit GHZ state, we need one Hadamard gate ('H' gate in the figure) and three pairwise entangling gates, which can be replaced by a single global four-qubit entangling gate. The phase gate ('S' gate) at the end of the first circuit is used to compensate for the phase difference between two circuit outputs. **b**, Experimental setup used for the implementation of the global entangling gate. Each ion in the trap encodes a qubit with energy splitting of ω_0, which is individually manipulated by Raman beams: a cover-all beam (blue) and an individual beam addressing a single ion (red). The individually addressed qubits are involved in the global entangling gate. **c**, Energy levels of $^{171}Yb^+$. The Raman beams (with detuning Δ) introduce a qubit-state-dependent force on each ion, with multiple motional modes driven simultaneously at a driving frequency of μ. The patterns of the collective motional modes in the transverse direction and their relative frequencies ν in the spectrum are shown in the inset. **d**, Implementation of the global entangling gate. With a single rectangular pulse, we cannot achieve uniform coupling strengths $\theta_{j,j'}$ on all of the qubit pairs owing to undesired inhomogeneous couplings (see also Methods). Instead, we can achieve uniform coupling by independently modulating the pulses on each ion.

equation (1) using the time evolution of equation (2), we have to close all of the motional trajectories and balance all of the coupling strengths, which lead to the following constraints

$$a_{j,m}(\tau) = 0 \tag{5}$$

$$\theta_{j,j'}(\tau) = \Theta \tag{6}$$

Considering a general situation with N qubits and M collective motional modes, there are $N \times M$ constraints from equation (5) and $\binom{N}{2}$ from equation (6). Therefore, we have to satisfy a total number of $N(N-1)/2 + NM$ constraints. In principle, we can fulfil the constraints by independently modulating the amplitude $\Omega_j(t)$ or the phase $\phi_j(t)$ of the Rabi frequency on each ion in a continuous or a discrete way. In the experimental implementation, we choose discrete phase modulation because we have high-precision controllability on the phase degree of freedom. We divide the total gate operation time into K segments with equal duration and independently modulate the phase on each ion in each segment, which provides $N \times K$ independent variables. Because of the nonlinearity of the constraints, it is challenging to find analytical solutions for the constraints of equations (5) and (6). Therefore, we construct an optimization problem to find numerical solutions. We minimize the objective function of $\sum_{j,m}|\alpha_{j,m}(\tau)|^2$ according to the constraints of equation (6)[21,27,28]. We note that we also use amplitude shaping at the beginning and the end of the operation to minimize fast-oscillating terms due to off-resonant coupling to the carrier transition[29]. Details about the constraints under discrete phase modulation and the construction of the optimization problem are provided in Supplementary Information. Moreover, we note that once we find the solution of the global N-qubit entangling gate, the entangling gate can be applied on any subset of qubits by simply setting $\Omega_j = 0$ for any qubit j outside the subset.

We experimentally implement the global entangling gates in a single linear chain of $^{171}Yb^+$ ions, as shown in Fig. 1b. A single qubit is encoded in the hyperfine levels of the ground-state manifold $^2S_{1/2}$, denoted as $|0\rangle \equiv |F=0, m_F=0\rangle$ and $|1\rangle \equiv |F=1, m_F=0\rangle$ (where F and m_F are the hyperfine and magnetic quantum numbers, respectively), with an energy gap of $\omega_0 = 12.642821$ GHz, as shown in Fig. 1c. The qubits are initialized to state $|0\rangle$ by optical pumping and measured using state-dependent fluorescence detection[30]. The fluorescence is collected by an electron-multiplying charge-coupled device (EMCCD) to realize a site-resolved measurement. After ground-state cooling of the motional modes, coherent manipulations of the qubits are performed by Raman beams produced by a picosecond-pulse laser[31]. One of the Raman beams is broadened to cover all of the ions, whereas the other is divided into several paths that are tightly focused on each ion (referred to as 'individual beam' hereafter). The cover-all beam and the individual beams intersect each other perpendicularly at the ion chain, and drive radial modes mainly along the x direction. Using a multi-channel acousto-optic modulator controlled by a multi-channel arbitrary waveform generator, we realize independent control of the individual beams on each ion, as illustrated in Fig. 1b, similarly to the setup of ref. [14]. Additional information about the experimental setup is provided in Methods.

To test the performance of the global N-qubit entangling gate, we use the $GE_N(\pi/4)$ gate to generate an N-qubit GHZ state and then measure the state fidelity. Starting from the product state $|0\ldots0\rangle$, the GHZ state can be prepared by applying the global entangling gate, while additional single-qubit σ_x rotations by $\pi/2$ are needed if N is odd. After the state preparation, we obtain the state fidelity by measuring the population of the entangled state and the contrast of the parity oscillation[32]. We also use the fidelity of the GHZ state to test the most important

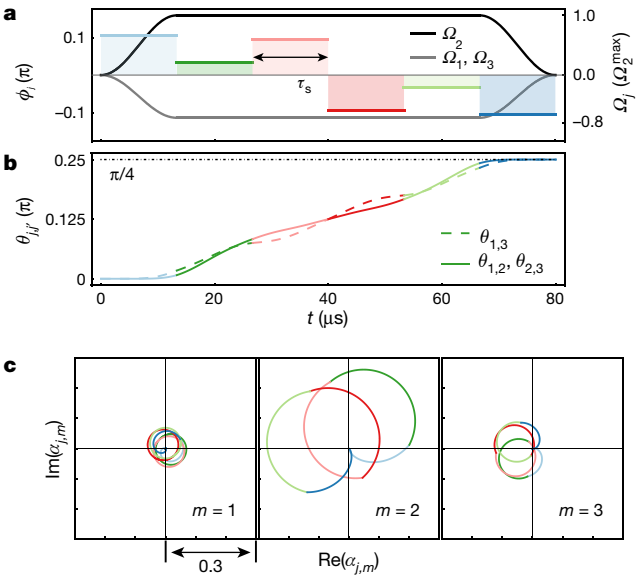

Fig. 2 | Experimental implementation of a global three-qubit entangling gate. a, Pulse scheme with phase and amplitude modulation. The phase ϕ_j is discretely modulated, as shown by the coloured lines. The specific values of the modulated phases are given in Methods. The amplitudes of the Rabi frequencies Ω_j, shown by the black and grey curves, are shaped at the beginning (end) of the gate operation using a sin-squared profile with switching time equal to the duration of a single segment, τ_S. We note that the additional π-phase shift of the middle ion is treated as a negative sign for Ω. **b**, Accumulation of coupling strength $\theta_{j,j'}$ over the evolution time. All of the coupling strengths increase to the desired value of π/4. **c**, Motional trajectories $\alpha_{j,m}$; the first qubit in phase space is shown as an example. Different colours correspond to the different segments in **a**.

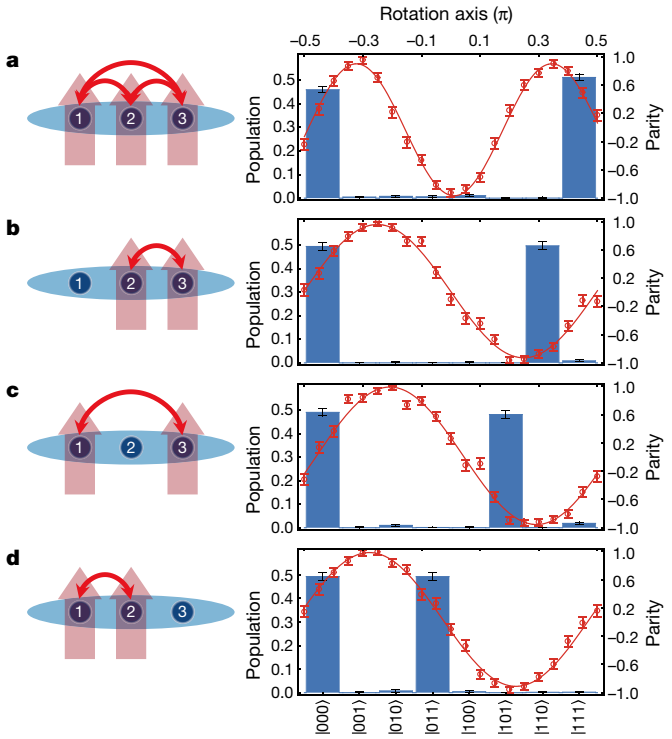

Fig. 3 | Experimental implementation and results of the global entangling gates in three-ion qubits. a–d, The left column shows the operation of the global entangling gate, which can generate entanglement of entire qubits (**a**) or any pair of qubits (**b–d**) by switching on the individual beams on the target ions without changing any modulated patterns. The right column shows the population (blue histogram) and the parity oscillation (red circles, experimental data; red curves, fitting results) of the generated GHZ state. The error bars indicate one standard deviation. **a**, Three-qubit GHZ state with a state fidelity of 95.2% ± 1.5%. **b–d**, Two-qubit GHZ states of qubit pairs (2, 3), (1, 3) and (1, 2), with fidelities of 96.7% ± 1.8%, 97.1% ± 1.9% and 96.5% ± 1.5%, respectively.

feature of the global entangling gate, that is, whether it can be applied on any subset of qubits that are addressed by individual laser beams without changing the modulation pattern.

As a first demonstration of the global entangling gate, we use three $^{171}Yb^+$ ions with the frequencies of the collective motional modes in the x direction $\{\nu_1, \nu_2, \nu_3\} = 2\pi \times \{2.184, 2.127, 2.044\}$ MHz. We choose the detuning μ between the last two modes to be $2\pi \times 2.094$ MHz. The total gate time is fixed at 80 μs and divided into six segments. The details of the phase modulation pattern and the ratio of the amplitude shaping of each ion to the centre one are shown in Fig. 2a. With these parameters, the constraints of equations (5) and (6) are fulfilled, as shown in Fig. 2b, c. We use this global three-qubit entangling gate to prepare the three-qubit GHZ state with a state fidelity of 95.2% ± 1.5% (all uncertainties are one standard deviation), as shown in Fig. 3a. Moreover, by turning off the individual beam on a qubit, we can remove the couplings between that qubit and other qubits, as shown in Fig. 3. In the three-qubit system, the global entangling gates on the subsets become pairwise gates on arbitrary qubit pairs, which are used to generate the two-qubit GHZ states with fidelities higher than 96.5% in the experiment, as shown in Fig. 3b, c.

For a further demonstration of the global entangling gate, we move to a four-qubit system with motional frequencies $\{\nu_1, \nu_2, \nu_3, \nu_4\} = 2\pi \times \{2.186, 2.147, 2.091, 2.020\}$ MHz. The larger system means more constraints, and more segments are required. To realize a global four-qubit entangling gate, we choose the detuning μ to be $2\pi \times 2.104$ MHz and fix the total gate time at 120 μs, which is evenly divided into twelve segments. The pulse scheme is shown in Fig. 4a, b. The number of the constraints in equation (6) increases quadratically with the number of qubits and reaches six in the four-qubit case, as shown in Fig. 4c.

By applying the global four-qubit entangling gate to all of the qubits, we successfully generate a four-qubit GHZ state with a state fidelity of 93.4% ± 2.0%, as shown in Fig. 4d. Similarly, we can prepare a three-qubit GHZ state or a two-qubit GHZ state by only addressing arbitrary three or two qubits, respectively. Experimentally, we choose the qubit set (2, 3, 4) to prepare the three-qubit GHZ state and the qubit pair (1, 3) to prepare the two-qubit GHZ state, with state fidelities of 94.2% ± 1.8% and 95.1% ± 1.6%, respectively, as shown in Fig. 4e, f.

All of the results are corrected to remove detection errors (see Methods). The state fidelities of all of the prepared GHZ states are mainly limited by fluctuations of the tightly focused individual beams and optical-path jittering of the Raman beams (2%–4%). Other infidelity sources in the experiment include drifting of the motional frequencies (1%–2%) and crosstalk of the individual beams with nearby ions (about 1%).

We have presented the experimental realization of global entangling gates, which can increase the efficiency of quantum circuits, using a scalable approach and a trapped-ion platform. The duration of a single global gate is comparable to that of a single pairwise gate with the same total number of ions[20]. Therefore, we clearly observe benefits of the global gates in terms of total gate counts and duration. Moreover, we theoretically optimize the pulse schemes for five and six qubits, and we find that the required number of segments and the gate duration increase linearly with the number of qubits. As long as the solutions to the optimization problem can be determined, we could extend and apply the global entangling gate to a higher number of qubits. Pulse optimization with a large number of qubits is an NP-hard problem, but it could be assisted by a classical machine-learning technique. Furthermore, we can extend the global entangling gate to a general form with arbitrary coupling strengths of $\{\theta_{j,j'}(\tau) = \Theta_{j,j'}\}$, which would further simplify quantum circuits for large-scale quantum computation and simulation[9]. During the preparation of this paper, we became aware of a related study about parallel pairwise entangling gates[33].

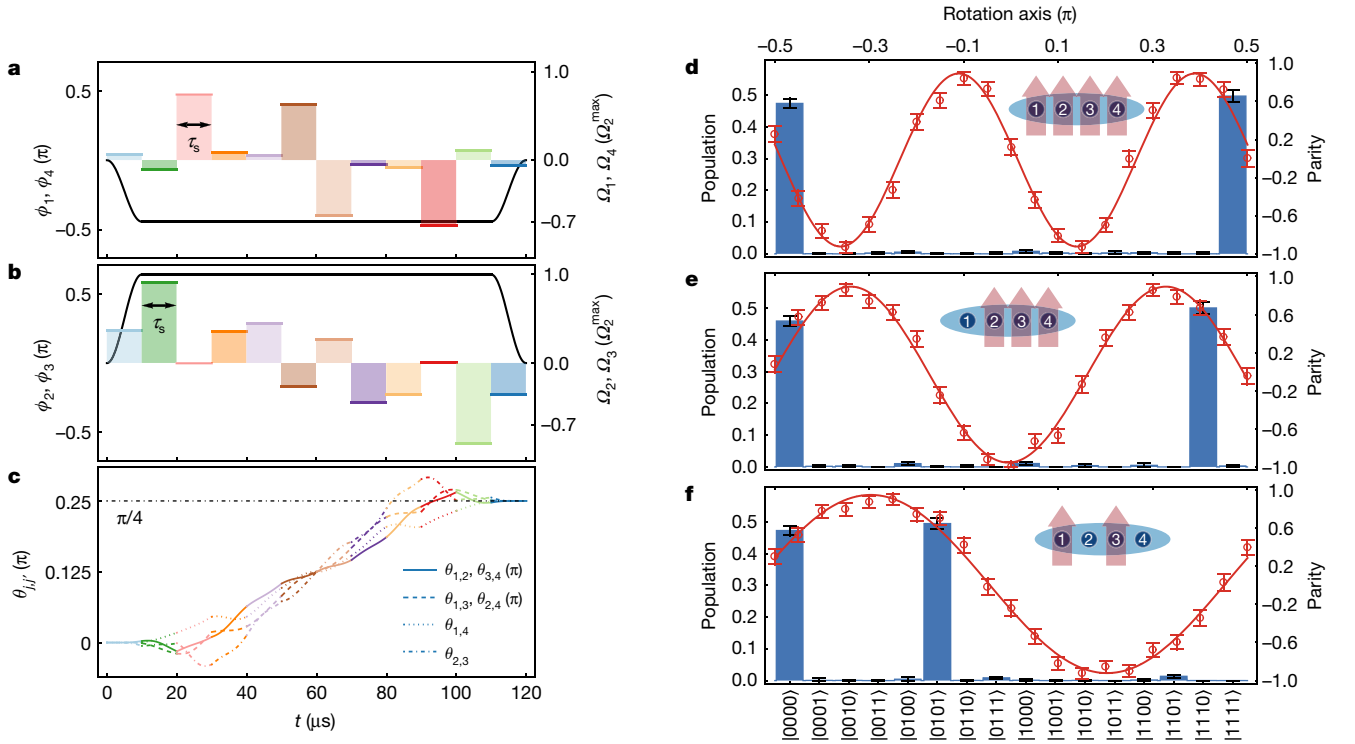

Fig. 4 | Experimental implementation and results of the global entangling gate in a four-ion system. a, b, Pulse scheme with phase and amplitude modulation. Using the symmetry of the system, we set the modulation patterns to be the same for the outer two qubits, (1, 4), and the inner two qubits, (2, 3). The additional π phase shift of each outer ion is treated as a negative sign for the amplitude Ω. The values of the modulated phases and the motional trajectories under this pulse scheme are given in Methods. **c**, Accumulation of coupling strengths $\theta_{j,j'}$ for all of the qubit pairs. The coupling strengths converge to the desired value of π/4 at the end of the gate. **d**–**f**, GHZ states prepared by the global entangling gates. By addressing an arbitrary subset of qubits—for example, (1, 2, 3, 4), (2, 3, 4) and (1, 3)—we can apply the entangling gate on the subset. The frequency of the parity oscillation, which is proportional to the number of addressed qubits, reveals that the prepared state is the GHZ state. Error bars indicate one standard deviation. The state fidelities of the prepared four-, three- and two-qubit GHZ states reach 93.4% ± 2.0%, 94.2% ± 1.8% and 95.1% ± 1.6%, respectively.

Online content

Any methods, additional references, Nature Research reporting summaries, source data, statements of data availability and associated accession codes are available at https://doi.org/10.1038/s41586-019-1428-4.

Received: 15 January 2019; Accepted: 10 May 2019;
Published online 24 July 2019.

1. Shor, P. W. Polynomial-time algorithms for prime factorization and discrete logarithms on a quantum computer. *SIAM J. Comput.* **26**, 1484–1509 (1997).
2. Feynman, R. P. Simulating physics with computers. *Int. J. Theor. Phys.* **21**, 467–488 (1982).
3. Lloyd, S. Universal quantum simulators. *Science* **273**, 1073–1078 (1996).
4. Nielsen, M. A. & Chuang, I. L. *Quantum Computation and Quantum Information* (Cambridge Univ. Press, 2010).
5. Casanova, J., Mezzacapo, A., Lamata, L. & Solano, E. Quantum simulation of interacting fermion lattice models in trapped ions. *Phys. Rev. Lett.* **108**, 190502 (2012).
6. Yung, M.-H. et al. From transistor to trapped-ion computers for quantum chemistry. *Sci. Rep.* **4**, 3589 (2015).
7. Ivanov, S. S., Ivanov, P. A. & Vitanov, N. V. Efficient construction of three- and four-qubit quantum gates by global entangling gates. *Phys. Rev. A* **91**, 032311 (2015).
8. Martinez, E. A., Monz, T., Nigg, D., Schindler, P. & Blatt, R. Compiling quantum algorithms for architectures with multi-qubit gates. *New J. Phys.* **18**, 063029 (2016).
9. Maslov, D. & Nam, Y. Use of global interactions in efficient quantum circuit constructions. *New J. Phys.* **20**, 033018 (2018).
10. Kim, K. et al. Entanglement and tunable spin–spin couplings between trapped ions using multiple transverse modes. *Phys. Rev. Lett.* **103**, 120502 (2009).
11. Britton, J. W. et al. Engineered two-dimensional Ising interactions in a trapped-ion quantum simulator with hundreds of spins. *Nature* **484**, 489–492 (2012).
12. Senko, C. et al. Coherent imaging spectroscopy of a quantum many-body spin system. *Science* **345**, 430–433 (2014).
13. Jurcevic, P. et al. Spectroscopy of interacting quasiparticles in trapped ions. *Phys. Rev. Lett.* **115**, 100501 (2015).
14. Debnath, S. et al. Demonstration of a small programmable quantum computer with atomic qubits. *Nature* **536**, 63–66 (2016).
15. Monz, T. et al. 14-qubit entanglement: creation and coherence. *Phys. Rev. Lett.* **106**, 130506 (2011).
16. Lanyon, B. P. et al. Universal digital quantum simulation with trapped ions. *Science* **334**, 57–61 (2011).
17. García-Ripoll, J. J., Zoller, P. & Cirac, J. I. Coherent control of trapped ions using off-resonant lasers. *Phys. Rev. A* **71**, 062309 (2005).
18. Zhu, S.-L., Monroe, C. & Duan, L.-M. Trapped ion quantum computation with transverse phonon modes. *Phys. Rev. Lett.* **97**, 050505 (2006).
19. Steane, A. M., Imreh, G., Home, J. P. & Leibfried, D. Pulsed force sequences for fast phase-insensitive quantum gates in trapped ions. *New J. Phys.* **16**, 053049 (2014).
20. Choi, T. et al. Optimal quantum control of multimode couplings between trapped ion qubits for scalable entanglement. *Phys. Rev. Lett.* **112**, 190502 (2014).
21. Leung, P. H. et al. Robust 2-qubit gates in a linear ion crystal using a frequency-modulated driving force. *Phys. Rev. Lett.* **120**, 020501 (2018).
22. Milne, A. R. et al. Phase-modulated entangling gates robust against static and time-varying errors. Preprint at https://arxiv.org/abs/1808.10462 (2018).
23. Schäfer, V. M. et al. Fast quantum logic gates with trapped-ion qubits. *Nature* **555**, 75–78 (2018).
24. Kaufmann, H. et al. Scalable creation of long-lived multipartite entanglement. *Phys. Rev. Lett.* **119**, 150503 (2017).
25. Haljan, P. C., Brickman, K.-A., Deslauriers, L., Lee, P. J. & Monroe, C. Spin-dependent forces on trapped ions for phase-stable quantum gates and entangled states of spin and motion. *Phys. Rev. Lett.* **94**, 153602 (2005).
26. Lechner, R. et al. Electromagnetically-induced-transparency ground-state cooling of long ion strings. *Phys. Rev. A* **93**, 053401 (2016).
27. Webb, A. E. et al. Resilient entangling gates for trapped ions. *Phys. Rev. Lett.* **121**, 180501 (2018).
28. Shapira, Y., Shaniv, R., Manovitz, T., Akerman, N. & Ozeri, R. Robust entanglement gates for trapped-ion qubits. *Phys. Rev. Lett.* **121**, 180502 (2018).
29. Roos, C. F. Ion trap quantum gates with amplitude-modulated laser beams. *New J. Phys.* **10**, 013002 (2008).
30. Olmschenk, S. et al. Manipulation and detection of a trapped Yb^+ hyperfine qubit. *Phys. Rev. A* **76**, 052314 (2007).
31. Hayes, D. et al. Entanglement of atomic qubits using an optical frequency comb. *Phys. Rev. Lett.* **104**, 140501 (2010).

32. Sackett, C. A. et al. Experimental entanglement of four particles. *Nature* **404**, 256–259 (2000).
33. Figgatt, C. et al. Parallel entangling operations on a universal ion trap quantum computer. *Nature* https://doi.org/10.1038/s41586-019-1427-5 (2019).

Acknowledgements This work was supported by the National Key Research and Development Program of China under grants 2016YFA0301900 and 2016YFA0301901 and the National Natural Science Foundation of China under grants 11574002 and 11504197.

Reviewer information *Nature* thanks Chris Ballance, Roee Ozeri and the other, anonymous, reviewer(s) for their contribution to the peer review of this work.

Author contributions Y.L., S.Z., K.Z., W.C. and Y.S. developed the experimental system. Y.L. and K.Z., together with J.-N.Z., investigated the theoretical schemes and optimized the pulse sequences. Y.L. and S.Z. obtained the data. K.K. supervised the project. Y.L. led the writing of the manuscript, with contributions from all authors.

Competing interests : The authors declare no competing interests.

Additional information
Extended data is available for this paper at https://doi.org/10.1038/s41586-019-1428-4.
Supplementary information is available for this paper at https://doi.org/10.1038/s41586-019-1428-4.
Reprints and permissions information is available at http://www.nature.com/reprints.
Correspondence and requests for materials should be addressed to Y.L. or K.K.
Publisher's note: Springer Nature remains neutral with regard to jurisdictional claims in published maps and institutional affiliations.

METHODS

Comparison of the single-mode and multimode approaches. We compare the single-mode and multimode approaches by numerically calculating the fidelities of GHZ states prepared using these two methods. In the model we only consider the effect of the COM mode and the second mode on a global gate with a radial trap frequency of $2\pi \times 2.18$ MHz and an axial trap frequency varying from $2\pi \times 0.5$ MHz (for three ions) to $2\pi \times 0.32$ MHz (for six ions). These values are consistent with the average experimental spacing of nearby ions of around 4.7 μm. It is difficult to perform a suitable quantum gate with a single axial COM mode at such low axial trap frequencies, owing to high heating rates and poor ground-state cooling, as the gate fidelity would be severely degraded with increasing number of ions. Therefore, we only consider the radial COM mode for the single-mode method.

For the radial COM mode method, we assume that bichromatic fields with detuning μ and time-independent Rabi frequency Ω are applied to all of the ion qubits. To close the trajectories of both modes simultaneously, we let δ_2/δ_1 be an integer r, where $\delta_m = \nu_m - \mu$. Under these assumptions, we can simplify equation (3) to the following form

$$\theta_{j,j'} = -\frac{\delta_1}{|\delta_1|}\frac{\pi(r-1)^2\eta_{\mathrm{COM}}^2\Omega^2}{(\Delta\nu)^2}\left(1+\frac{\eta_{j,2}\eta_{j',2}}{r\eta_{\mathrm{COM}}^2}\right) \tag{7}$$

where $\Delta\nu = |\nu_1 - \nu_2|$ is the frequency difference of the two modes. The gate duration is $\tau = 2\pi|\delta_1|^{-1} = 2\pi|r-1|(\Delta\nu)^{-1}$. An inhomogeneous $\eta_{j,2}$ would imbalance the coupling strengths, as shown in Fig. 1d, for example. We numerically evaluate the fidelities of the created GHZ states by calculating $\mathrm{Fid} = \langle|0\ldots0|\mathrm{GE}_N^{\dagger}(\pi/4)\exp[-i\sum_{j<j'}\theta_{j,j'}\sigma_x^j\sigma_x^{j'}]|0\ldots0\rangle|^2$. The results are summarized in Extended Data Fig. 1. As shown in the figure, to achieve a certain value of state fidelity, the minimal gate duration increases as $N^{2.4}$ with increasing number of ions. We note that we do not include other modes in the simulation, as the inclusion of all modes would lead to further decrease of the fidelity. By contrast, in our multimode approach, we consider the effects of all of the modes. The gate duration increases almost linearly with the number of ions, with unity representing the theoretical fidelity. A shorter gate duration than that of the single-mode approach would suppress the infidelities resulting from the limited coherence time, Raman scattering, motional heating and so on.

Experimental setup. In the experiment the single ion chain is held in a blade trap, in the geometry shown in Extended Data Fig. 2. The average spacing of nearby ions is around 4.7 μm. The Raman beams are produced by a picosecond-pulse laser with a centre wavelength of 377 nm and a repetition rate of about 76 MHz. The ion fluorescence is collected by an objective lens from the top re-entry viewport and then imaged with the EMCCD. The average detection fidelity is 96% for a single ion. The measured population of state, denoted as $P^{\mathrm{meas}} = \{p_{0\ldots0}, \ldots, p_{1\ldots1}\}$, where p_i is the probability of state $|i\rangle$, is calibrated to remove detection errors using the method described in ref. [34], which has been applied to many other experimental demonstrations[12,35]. The matrix of the detection errors (M) is determined experimentally and can be used to reconstruct the real population of the state, $P^{\mathrm{real}} = M^{-1}P^{\mathrm{meas}}$. However, to avoid non-physical results, we utilize the maximum-likelihood method to estimate the real population by minimizing the 2-norm $||P^{\mathrm{meas}} - MP^{\mathrm{real}}||_2$.

Experimental parameters. Here we present the details of the experimental pulse schemes for the global three- and four-qubit entangling gates. The maximal amplitudes of the Rabi frequencies are given using the theoretical Lamb–Dicke parameters

$$\eta_{j,m} = b_{j,m}\frac{2\sqrt{2}\pi}{\lambda}\sqrt{\frac{\hbar}{2M_{\mathrm{Yb}}\nu_m}} \tag{8}$$

where $b_{j,m}$ is the element of the normal-mode transformation matrix for ion j and motional mode m (ref. [36]), λ is the centre wavelength of the Raman laser, $\hbar$ is the reduced Planck constant and M_{Yb} is the mass of the $^{171}\mathrm{Yb}^+$ ion. For the COM mode, we have typically $\eta \approx 0.08/\sqrt{N}$ for any j in our setup, where N is the number of ions. The values of the modulated phases and amplitudes of the Rabi frequencies obtained from the optimization are shown in Extended Data Tables 1, 2.

In Fig. 2c we show the trajectories of the motional modes in the phase space for the three-qubit situation. In Extended Data Fig. 3, we show the motion trajectories of $\alpha_{j,m}(t)$ for the four-qubit case.

Data availability

All relevant data are available from the corresponding authors upon request.

34. Duan, L.-M. & Shen, C. Correcting detection errors in quantum state engineering through data processing. *New J. Phys.* **14**, 1778–1782 (2012).
35. Richerme, P. et al. Non-local propagation of correlations in quantum systems with long-range interactions. *Nature* **511**, 198–201 (2014).
36. James, D. F. V. Quantum dynamics of cold trapped ions with application to quantum computation. *Appl. Phys. B* **66**, 181–190 (1998).

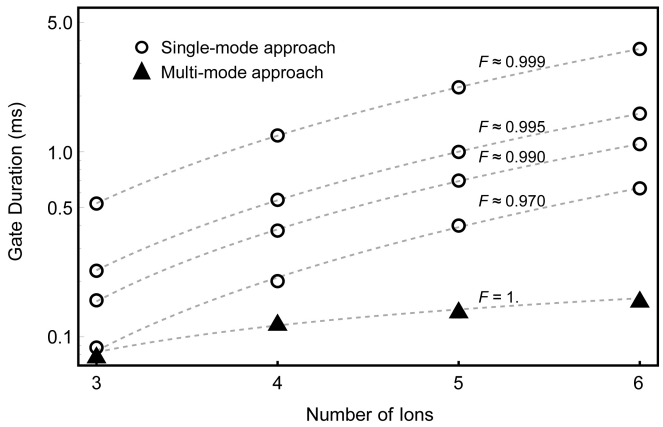

Extended Data Fig. 1 | Comparison between gate durations of single- and multi-mode approaches. For the given trap frequencies, the gate duration τ of the single-mode approach grows faster than linearly ($\tau \approx N^{2.4}$) to maintain the fidelity F when the number of ions, N, increases. The gate duration of the multi-mode approach grows near linearly, with a theoretical fidelity of unity. The vertical axis is on a logarithmic scale.

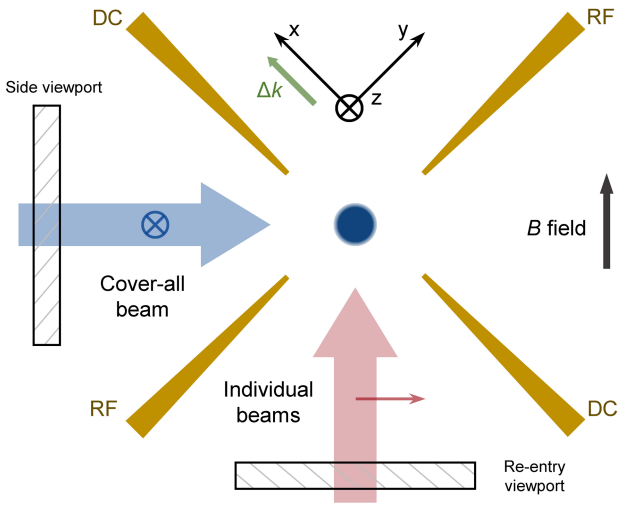

Extended Data Fig. 2 | Side view of the experimental ion-trap system. The figure shows the structure of the blade trap. The radiofrequency potential is applied to the RF electrodes and the direct-current (DC) electrodes are connected to the direct-current potential. A static magnetic field of $B \approx 6 \times 10^{-4}$ T is applied along the direction shown in the figure. The cover-all beam goes through the side viewport and is focused at the ion-chain position into an elliptical Gaussian beam, with waists of about 30 μm along the ion chain and about 5 μm in the perpendicular direction. The individual beams go through the bottom re-entry viewport and have a focused radius of about 1 μm at the ion position. The average laser power is around 120 mW for the cover-all beam and around 1 mW for each individual beam. The effective wave vector Δk of the two Raman beams is almost in the x direction, and the beams are polarized linearly, perpendicular to each other.

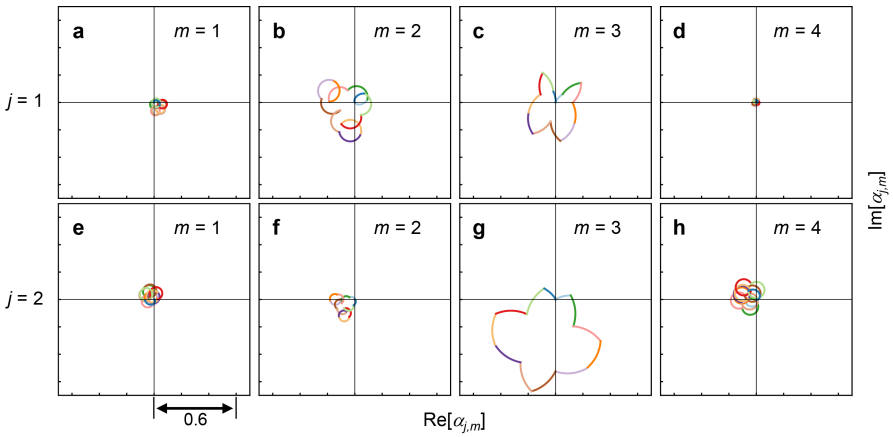

Extended Data Fig. 3 | Motional trajectories in phase space for the global four-qubit entangling gate. Because we apply different modulated-phase patterns to the qubits (1, 4) and (2, 3), the shapes of the motional trajectories in **a**–**d** and **e**–**h** are different.

Extended Data Table 1 | Pulse scheme for the global three-qubit entangling gate

Qubit j		1	2	3
Ω_j^{max} (MHz)		$-2\pi \times 0.181$	$2\pi \times 0.253$	$-2\pi \times 0.181$
$\phi_{j,k}$ (π)	1	0.104	0.104	0.104
	2	0.033	0.033	0.033
	3	0.095	0.095	0.095
	4	-0.095	-0.095	-0.095
	5	-0.033	-0.033	-0.033
	6	-0.104	-0.104	-0.104

Here, Ω_j^{max} refers to the maximal amplitude of the Rabi frequency on the jth qubit during pulse shaping and $\phi_{j,k}$ refers to the value of the modulated phase on the jth qubit in the kth segment.

Extended Data Table 2 | Pulse scheme for the global four-qubit entangling gate

Qubit j		1	2	3	4
Ω_j^{max} (MHz)		$-2\pi \times 0.117$	$2\pi \times 0.168$	$2\pi \times 0.168$	$-2\pi \times 0.117$
$\phi_{j,k}$ (π)	1	0.041	0.231	0.231	0.041
	2	-0.070	0.579	0.579	-0.070
	3	0.472	-0.001	-0.001	0.472
	4	0.054	0.230	0.230	0.054
	5	0.035	0.285	0.285	0.035
	6	0.402	-0.170	-0.170	0.402
	7	-0.402	0.170	0.170	-0.402
	8	-0.035	-0.285	-0.285	-0.035
	9	-0.054	-0.230	-0.230	-0.054
	10	-0.472	0.001	0.001	-0.472
	11	0.070	-0.579	-0.579	0.070
	12	-0.041	-0.231	-0.231	-0.041

The definitions of Ω_j^{max} and $\phi_{j,k}$ are as in Extended Data Table 1.